Mon. Not. R. Astron. Soc. **000**, 1–10 (2012) Printed 5 May 2014 (MN LATEX style file v2.2)

Blocking low-eccentricity EMRIs: A statistical direct-summation $N-$body study of the Schwarzschild barrier

Patrick Brem[1] ⋆, Pau Amaro-Seoane[1] & Carlos F. Sopuerta[2]
[1] *Max Planck Institut für Gravitationsphysik (Albert-Einstein-Institut), D-14476 Potsdam, Germany*
[2] *Institut de Ciències de l'Espai (CSIC-IEEC), Facultat de Ciències, Campus UAB, Torre C5 parells, 08193 Bellaterra, Spain*

draft 5 May 2014

ABSTRACT
The capture of a compact object in a galactic nucleus by a massive black hole (MBH), an extreme-mass ratio inspiral (EMRI), is the best way to map space and time around it. Recent work on stellar dynamics has demonstrated that there seems to be a complot in phase space acting on *low-eccentricity* captures, since their rates decrease significantly by the presence of a blockade in the rate at which orbital angular momenta change takes place. This so-called "Schwarzschild barrier" is a result of the impact of relativistic precession on to the stellar potential torques, and thus it affects the enhancement on lower-eccentricity EMRIs that one would expect from resonant relaxation. We confirm and quantify the existence of this barrier using a statistical sample of 2,500 direct-summation $N-$body simulations using both a post-Newtonian and also for the first time in a direct-summation code a geodesic approximation for the relativistic orbits. The existence of the barrier prevents low-eccentricity EMRIs from approaching the central MBH, but high-eccentricity EMRIs, which have been wrongly classified as "direct plunges" until recently, ignore the presence of the barrier, because they are driven by two-body relaxation. Hence, since the rates are significantly affected in the case of low-eccentricity EMRIs, we predict that a LISA-like observatory such as eLISA will predominantly detect high-eccentricity EMRIs.

Key words: Stellar dynamics – Extreme-Mass-Ratio Inspirals – Schwarzschild barrier – post-Newtonian dynamics.

1 INTRODUCTION

Massive black holes (MBHs), with masses ranging from some $10^4\,M_\odot$ to a few $10^9\,M_\odot$ are very likely present in the centre of most galaxies. Measurements of the kinematics of gas and stars in the central regions of nearby galaxies (see e.g. de Zeeuw 2001; Barth 2004; Kormendy 2004; Richstone 2004) have provided us with compelling evidence. Our own Milky Way (MW) is the galaxy for which we have the strongest observational proof a central MBH. Data based on 16 years of observations set the mass of the central SMBH to $\sim 4\times10^6\,M_\odot$ (Eisenhauer et al. 2005; Ghez et al. 2005, 2008; Gillessen et al. 2009; Genzel et al. 2010).

To interact with the central MBH, stars have to find themselves on "loss-cone" orbits, which are orbits elongated enough to have a very close-in pericentre (Frank & Rees 1976; Lightman & Shapiro 1977; Amaro-Seoane & Spurzem 2001). While main-sequence stars are tidally disrupted when approaching the central massive black hole (MBH), compact objects (stellar black holes, neutron stars, and white dwarfs) slowly spiral into the MBH via the gradual loss in the form of gravitational radiation and are eventually swallowed after some $\sim 10^{3-5}$ orbits in the eLISA band(Amaro-Seoane et al. 2007, 2012a,b; Amaro-Seoane 2012). This is the best way to probe general relativity (Sopuerta 2010) and, thus, the factory of space and time around a massive black hole. We will also get additional information about the binary itself: in particular the masses of the system and the spins of the MBH can be measured to a level of precision without any precedent (see Amaro-Seoane et al. 2007,and references therein). Besides, the detection will provide us with information about the distribution of dark objects in galactic nuclei and globular clusters.

Producing EMRIs is more difficult than producing tidal disruptions of stars (e.g., Rees 1988; Magorrian & Tremaine 1999; Syer & Ulmer 1999; Wang & Merritt 2004) because while disruptions require a single passage within a critical radius, an EMRI is a progressive phenomenon that is only

⋆ E-mail: Patrick.Brem@aei.mpg.de

successful if the small compact object suffers a large number of close encounters with the central MBH.

The requirement for an EMRI to be successful is not just to have a small periapsis, but that the gravitational radiation timescale is sufficiently shorter than 2-body relaxation, which could have a significant impact on the periapsis. Although the basic ideas are explained in detail in the recent review of Amaro-Seoane (2012), we deem it important to briefly summarize in the next paragraphs the fundamentals of the ideas of two different categories of EMRIs, since this will be crucial to understand the main results of this paper.

In a galactic nucleus without dissipation processes a star suffers "gravitational tugs" in the regime where the evolution is dominated by close encounters with other stars. These tugs, since they are driven by two-body relaxation, are *random* and originated by interacting with other stars that happen to have a very close position. The scattering rate is very similar in orbital energy E and angular momentum L. If the star gets close to a very low L, which is statistically probable, then the picture changes: The rate at which the star changes L will be much shorter than that at which it changes E. If we introduce a dissipation term in the picture, e.g. gravitational waves, the star follows the same initial evolution and, at some point, our test star, the compact object, reaches the region in which it is on a very radial orbit. In this case, at every periapsis passage, the test star loses a significant amount of energy and, hence, the semi-major axis shrinks. If the process is efficient enough it becomes an EMRI.

Stars in very radial orbits would then scatter faster in L than in E, so that they would end up as direct plunges, i.e. being swallowed by the MBH after an insignificant amount of gravitational wave bursts. Although their event rate is much larger, they do not allow us to get a full picture of the scenario as complete as compared with the slow inspiral of an EMRI (but see the recent work of Berry & Gair 2012,on bursting sources). The threshold lies around $\sim 10^{-2}$ pc (Hopman & Alexander 2005) and this is what has led up to now to the thought that the EMRI event rate should be dominated by the physical phenomena happening in the innermost volume around the MBH, of radius $\sim 10^{-2}$ pc.

However, while this is strictly true for Schwarzschild MBHs, *the situation for spinning MBHs drastically changes the narrative*. Recently, Amaro-Seoane et al. (2012d) proved that for Kerr MBHs plunges do not plunge, but spend a very large number of cycles in the eLISA band. I.e. they are simply high-eccentricity EMRIs. The authors prove that the event rate of both high-eccentric and also low-eccentric EMRIs is enhanced by the spin as compared to the Schwarzschild case by an amount that depends on the specific eccentricity and inclination of the orbit.

The fact that compact objects on a "plunge" orbit have been envisaged as uninteresting has led to an effort to understand the phenomena that could lead to the creation of EMRIs in a volume of radius $\sim 10^{-2}$ pc. In this volume, resonant relaxation is very likely the most important process to lead compact objects to EMRI orbits (Hopman & Alexander 2006). Nonetheless, while in the absence of relativistic effects resonant relaxation is expected to change the angular momentum of the stellar BHs very efficiently, (Merritt et al. 2011, hereafter MAMW11) showed recently with a few direct $N-$body experiments that introducing relativistic precession effects are both a blessing and a curse for the inspiral event rate: RR is quenched at high eccentricities, resulting in more inspirals than plunges. However, this quenching also means that, in total, fewer BHs will reach pericentres that are small enough to lead to an inspiral observable by gravitational wave detectors such as eLISA (Amaro-Seoane et al. 2012a,b). In this paper we present a statistical study of the Schwarzschild barrier (SB) with a set of 2,500 direct-summation $N-$ body simulations including relativistic corrections to study and quantify this effect. We implement the relativistic effects using a post-Newtonian formalism as in Kupi et al. (2006) but also, and *for the first time ever in a direct-summation integrator, a geodesic scheme.*

This paper is organized as follows: In Section 2 we present the physical setup and the numerical methods used. In Section 3 we present general results and discuss the implications for the Schwarzschild barrier in Section 4.

2 PHYSICAL SETTING AND NUMERICAL METHODS

Recently, MAMW11 estimated with a few direct-summation N-body simulations expanded with a statistical Monte-Carlo study that the traditional EMRI event rate is markedly decreased by the presence of a blockade in the rate at which orbital angular momenta change takes place. This so-called Schwarzschild barrier is a result of the impact of relativistic precession on to the stellar potential torques. Although the authors find that some particles can penetrate the barrier, EMRIs are significantly suppressed in this scenario.

In analogy to MAMW11, the setup we consider consists of a central MBH of mass $M_\bullet$ surrounded by 50 stellar mass black holes (BHs) of mass $m_\star$. We fix the masses of the MBH and the stellar black holes at

$$M_\bullet = 10^6\, M_\odot\,, \qquad m_\star = 50\, M_\odot\,. \tag{1}$$

Initially we distribute the stars in phase space following a distribution of the form $N(a, e^2)\, da\, de^2 = N_0 da\, de^2$, with a the semi-major axis of the BHs and e their eccentricity. The semi-major axes range between 0.1 mpc $< a <$ 10 mpc.

This setup represents roughly a relaxed distribution of stellar mass objects around a MBH (Freitag et al. 2006). We note that the event rates we obtain in this study are only applicable to this specific, idealized system where $N =$ 50 heavy, equal mass stellar BHs orbit a MBH. For more realistic estimates one would need to take into account other properties of galactic nuclei, such as the stellar background, a certain mass distribution and larger N.

2.1 Timescales

In order to have EMRI events, one needs BHs on orbits with pericentres of only a few gravitational radii ($r_g = GM_\bullet/c^2$). This requires the existence of physical mechanisms for driving BHs from their initial orbits onto very eccentric ones.

A purely Newtonian system has two different ways of exchanging angular momentum L (or eccentricity e) and orbital binding energy E (or semi-major axes a). The first one

is by two-body scattering, or non-resonant relaxation (NR) (see e.g. Spitzer 1987; Binney & Tremaine 2008; Amaro-Seoane 2012). Every time two objects come close they undergo scattering, changing the momenta of the scattering partners. This very basic mechanism exists in all gravitationally interacting systems from compact star clusters to galaxies. The associated time-scale for changing the angular momentum L of a given particle by $\Delta L \sim L$ is

$$\tau_{\rm NR} = 4.6\,{\rm Myr}\,\tilde{a}^{1/2}\Big(\frac{M_\bullet}{10^6\,M_\odot}\Big)^{3/2}\Big(\frac{m}{50\,M_\odot}\Big)^{-2}\Big(\frac{N_{<1}}{5}\Big)^{-1}, \tag{2}$$

where $N_{<1}$ is the number of stars within a sphere of 1 mpc and $\tilde{a}$ will denote the semi-major axis in mpc throughout the rest of the paper. The derivation of this equation, although trivial, can be found in MAMW11.

In Newtonian systems with a central massive object which dominates the gravitational potential, however, this relaxation mechanism is usually dominated by resonant relaxation (RR) (Hopman & Alexander 2006).

The torque of a spherical distribution of stars of mass $M_\star(r<a)$ inside a sphere of radius r on a BH with semi-major axis a leads to a retrograde orbital in-plane precession on a time-scale

$$\tau_{\rm M} = \frac{2\pi}{g(e)M_\star(r<a)}\Big(\frac{M_\bullet a^3}{G}\Big)^{1/2}, \tag{3}$$

where the eccentricity dependent function $g(e)$ is given by

$$g(e) = \frac{1+\sqrt{1-e^2}}{2\sqrt{1-e^2}}\,. \tag{4}$$

¿From Eq. (3) we can derive the time-scale of changes in the angular momentum, which for our system is given by

$$\tau_{\rm RR} \approx \frac{5.9\times10^4\,{\rm yr}}{\beta_s^2 g(e)}\Big(\frac{M_\bullet}{10^6\,M_\odot}\Big)^{1/2}\Big(\frac{m_\star}{50\,M_\odot}\Big)^{-1}\tilde{a}^{3/2}, \tag{5}$$

where β_s is a factor of order unity. For the derivation of Eq. (5) we defer the reader to reference MAMW11. This mechanism for relaxation, RR, is much more efficient than NR *at these distances* because the particles interact through coherent torques in resonant Keplerian orbits. It therefore could lead in principle to an enhancement in the EMRI event rate.

Relativistic effects introduce two new time-scales. The conservative Schwarzschild precession, appearing in particular at the first and second post-Newtonian orders, causes a precession of the pericentre by an angle

$$\delta\Phi = \frac{3\pi G M_\bullet}{c^2}\frac{1}{a(1-e^2)} \tag{6}$$

per orbit. This leads to the following associated time-scale

$$\tau_{\rm SS} = \frac{\pi}{\delta\Phi}P(a) = \frac{2\pi c^2}{3(GM_\bullet)^{3/2}}a^{5/2}(1-e^2), \tag{7}$$

where $P(a) = 2\pi(a^3/GM_\bullet)^{1/2}$ is the orbital period. In a more convenient notation this yields

$$\tau_{\rm SS} \approx (2\times10^4\,{\rm yr})\,\tilde{a}^{5/2}(1-e^2)\Big(\frac{M_\bullet}{10^6\,M_\odot}\Big)^{-3/2}. \tag{8}$$

The second important time-scale is the inspiral time $\tau_{\rm GR}$ via gravitational radiation only which, for high eccentricities ($e\simeq1$), is given by (Peters 1964)

$$\tau_{\rm GW} \approx \frac{5c^5}{256G^3}\frac{a^4}{m_\star M_\bullet(m_\star+M_\bullet)}(1-e^2)^{7/2} \tag{9}$$

$$\approx (1.16\times10^{13}\,{\rm yr})\,\tilde{a}^4(1-e^2)^{7/2} \times\Big(\frac{m_\star}{50\,M_\odot}\Big)^{-1}\Big(\frac{M_\bullet}{10^6\,M_\odot}\Big)^{-2}, \tag{10}$$

for $M_\bullet \gg m_\star$. This timescale is highly sensitive to the eccentricity and semi-major axis and for a typical BH in the system much longer than any other relevant time. However, for particles very close to the central MBH, gravitational radiation may drive them gradually into the capture radius leading to an "inspiral event".

2.2 A direct-summation code with post-Newtonian and geodesic corrections

In order to integrate the initial configuration over time we use the publicly available `planet` code by Sverre Aarseth (Aarseth 1999, 2003), a direct summation $N-$body integrator. We have modified this code in order to introduce relativistic corrections to the Newtonian acceleration (Amaro-Seoane et al. 2012c). For the studies that we present here we have considered the following types of dynamics:

- purely Newtonian dynamics
- post-Newtonian (PN) corrections
- relativistic geodesic equations for motion of the particles around the MBH

In the purely Newtonian case, the integration is obviously done without modifications to the acceleration equations. In the second case we add the PN corrections in the following way:

$$F = \overbrace{F_0}^{\rm Newt.} + \overbrace{\underbrace{c^{-2}F_2}_{\rm 1PN} + \underbrace{c^{-4}F_4}_{\rm 2PN}}^{\rm periapsis\ shift} + \overbrace{\underbrace{c^{-5}F_5}_{\rm 2.5PN}}^{\rm energy\ loss} + \overbrace{\mathcal{O}(c^{-6})}^{\rm neglected}, \tag{11}$$

where the individual F_i's denote the different PN corrections to the total force on a particle, which can be found in Appendix B.

Given the high mass ratios involved in EMRIs, their motion around a MBH can be also approximated by solving the geodesic equations of motion, neglecting in this way dissipative effects due to gravitational wave emission and higher-order corrections in the mass ratio. In our case, the geodesic equations describe the exact trajectory of a test mass particle around a Schwarzschild MBH. *Unlike the PN approximation, the geodesic equations are valid even in the last few r_g during a plunge or inspiral*, however only in the limit $m_\star/M_\bullet \to 0$. Some orbits are expected to migrate towards plunge or inspiral orbits at pericentre distances of $r_p < 15\,r_g$, where the errors of the PN approximation can already be quite significant (Yunes & Berti 2008). In order to

test the existence of the Schwarzschild barrier at small distances, we have implemented these corrections in the `planet` code.

Since the geodesic equations do not contain dissipative terms we compare the results of using them with the conservative PN implementations, i.e. setting the dissipative correction $F_5 = 0$ in Eq. (11).

At any given time all the active acceleration corrections are computed only between the MBH and a stellar BH object. The semi-major axis and eccentricity evolution is tracked by monitoring the distances at periapsis $r_{\rm min}$ and apoapsis $r_{\rm max}$ using the standard relations

$$a = \frac{r_{\rm max} + r_{\rm min}}{2}\,, \tag{12}$$

$$e = \frac{r_{\rm max} - r_{\rm min}}{r_{\rm max} + r_{\rm min}}\,, \tag{13}$$

which are valid for any acceleration correction. This calculation does not require a PN expansion of the Keplerian expressions for a and e and is thus consistent with the purely Newtonian, PN and geodesic equations of motion.

We record a merger event whenever a particular has an instantaneous separation to the MBH of $r < 6\,r_g$ (i.e. the Schwarzschild last stable orbit for circular orbits). We note that MAMW11 use $r < 8\,r_g$ and thus might classify a few events that we call inspirals as plunges. We run $N_P = 500$ simulations of the models described above, with different random seeds for the distribution of stars, for a few Myr or until a merger event happens.

3 RESULTS FROM THE SIMULATIONS

For all the different sets P of simulations we will compute the average time $\tau_{X,P}$ for the occurrence of a certain event X in the simulation set P in the following way:

$$\tau_{X,P} = \sum_{i=1}^{N_P} T_{i,P} \cdot \frac{1}{K_{X,P}}\,, \tag{14}$$

where the sum runs over all the total duration times $T_{i,P}$ of the N_P simulations and $K_{X,P}$ gives the total number of events X in the set P. Every simulation has been given a burn-in time of $10^4\,$yr, which is of the order of $\tau_{\rm RR} \approx 6\times10^4\,$yr (see Eq. 5) in order to discard merger events due to particles being created extremely close to the MBH or even within the capture radius by the randomization routine.

In Eq. (14), the possible events X can be either i for an inspiral event or p for a plunge event. We define the error for our results as the Poisson error,

$$\sigma_{X,P} = \sqrt{K_{X,P}}\,. \tag{15}$$

The criterion for an event to be an inspiral event is taken to be

(i) $\mathrm{a_{cap}} < 1\,$mpc and
(ii) $\mathrm{a_{cap}} < 1.5\,\mathrm{a}(t_{\rm cap} - 500\,{\rm yr})$.

The second condition ensures that the semi-major axis of the merging body ($\mathrm{a_{cap}}$) has shrunk significantly prior to capture in order to dismiss plunges with low semi-major axis. The choice of 500 years has empirically proven to distinguish perfectly between plunges and inspirals.

3.1 Newtonian Simulations (Set SI)

In this section we present the results for our study using only purely Newtonian accelerations, i.e. only the term F_0 in Eq. (11). In this case, the individual objects exchange energy and angular momentum efficiently via resonant relaxation (RR). For the plunge time, using Eq. (14), we find

$$\tau_{\rm p,I} = (3.7 \pm 0.2) \times 10^4\,{\rm yr}\,. \tag{16}$$

This agrees very well with the RR timescale given by Eq. (5) for a typical particle, which confirms that this is the dominant mechanism at these radii for driving stellar objects into the central body in the purely Newtonian case. Of course, we do not identify any inspirals in the absence of gravitational radiation effects.

3.2 Simulations including 2.5PN corrections (Set SII)

We now add only the dissipative effects due to gravitational radiation emission, which appear at 2.5 PN order, to the acceleration equations.

The analysis of the simulations now gives

$$\tau_{\rm p,II} = (3.8 \pm 0.2) \times 10^4\,{\rm yr}\,, \tag{17}$$

$$\tau_{\rm i,II} = (2.3 \pm 0.4) \times 10^5\,{\rm yr}\,. \tag{18}$$

Now, with the inclusion of the effects of gravitational radiation, gradual inspirals into the MBH are possible. This converts a subset of the plunge events from the simulations in set SI into inspiral events. However, the inspiral time $\tau_{\rm GW}$ given by Eq. (10) only becomes smaller than the RR time for

$$a(1-e) \lesssim 5\,r_g\,, \tag{19}$$

which is smaller than the assumed capture radius. Thus, the efficient RR still drives the majority of particles into the capture radius before they can decouple from the stellar background and undergo a clean inspiral. In other words, the transfer of angular momentum to more eccentric orbits by RR is faster than the circularization by the dissipative 2.5PN term.

3.3 Simulations including 1PN, 2PN and 2.5PN corrections (Set SIII)

In this set of simulations we include all PN terms up to 2.5PN order in our calculations. This introduces prograde Schwarzschild precession in addition to the dissipation produced by gravitational-wave emission. This effect is expected to increase the associated times for inspiral and plunges, since it eliminates efficient RR at high eccentricities. We find

$$\tau_{\rm p,III} = (1.3 \pm 0.2) \times 10^6\,{\rm yr}\,, \tag{20}$$

$$\tau_{\rm i,III} = (2.0 \pm 0.4) \times 10^6\,{\rm yr}\,. \tag{21}$$

As expected, the inspiral and plunge times are now of the order of a two-body relaxation time, Eq. (2). We also see that the substantial difference between plunge and inspiral times seen in SII vanishes, because now the relaxation time-scale is much higher and gravitational radiation can more easily decouple the star from the stellar background. Compared to the previous set now the 2.5PN term is able to circularize and shrink the BH orbit faster than classical relaxation increases eccentricity.

3.4 Simulations including 1PN and 2PN corrections (Set SIV)

In order to compare our PN results with the results using geodesic equations of motion, we also ran a set of simulations with only the conservative 1PN and 2PN terms. In this set we find a plunge time of

$$\tau_{\rm p,IV} = (6.6 \pm 0.5) \times 10^5 \,{\rm yr}\,. \tag{22}$$

This is consistent with the time we would obtain from SIII when combining plunge and inspiral events and shows again that the 2.5PN term does not change the important mechanisms for angular momentum transfer.

3.5 Simulations considering geodesic motion around the MBH (Set SV)

In this set of simulations we investigate the system using Newtonian forces to describe the gravitational interactions between the stellar black holes and to describe the interaction between the MBH and individual stellar black holes we use the exact solution of the motion of a test mass in a Schwarzschild metric (geodesic motion). This does intrinsically exclude dissipative effects and therefore, the results of this subsection should be compared to those from the set SIV. In the limit of $m_\star \ll M_\bullet$, the geodesic equations (in harmonic coordinates) expanded up to 2PN order and the conservative 2PN equations agree (see Appendix A), and hence they are consistent descriptions at this level of approximation.

In this set of simulations we obtain

$$\tau_{\rm p,V} = (7.1 \pm 0.7) \times 10^5 \,{\rm yr}, \tag{23}$$

which is consistent with $\tau_{\rm p,IV}$. This agreement means that the motion very close to the MBH is not relevant for the relaxation processes that drive BHs into plunge orbits.

4 SCHWARZSCHILD BARRIER

In order to quantify the nature of the "Schwarzschild barrier", we first plot the normalized presence density. This is a measure of the total time any particle spends in a certain logarithmic bin in $(a, 1-e)$, summed up over all particles and simulations. For comparison with the next figures, in figure 1 we depict the theoretical distribution that we can expect from a power-law of exponent $\gamma = 1.75$. Next, we show the histogram for the Newtonian case, Fig. 2 (top panel) and the relativistic case (bottom panel). If we consider our specific setup, there are 3 different regions in the $(a, 1-e)$ plane where different mechanisms are efficient. In the right-most

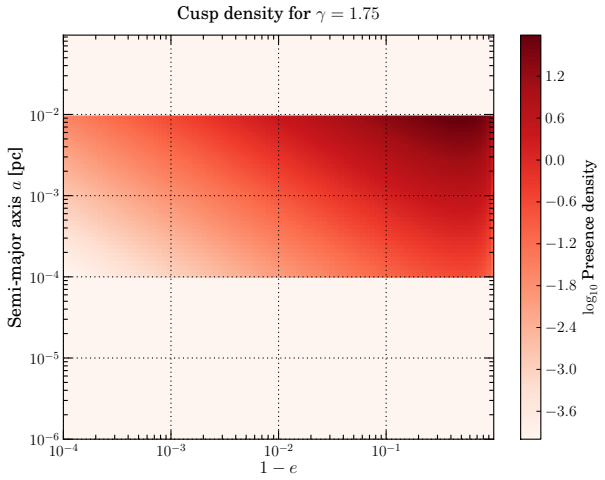

Figure 1. Theoretical distribution of a truncated cusp of $\gamma = 1.75$

region, where pericentres are large, RR plays the dominant role. The left border of this region is roughly given by the appearance of the Schwarzschild precession which inhibits the BHs from experiencing coherent torques. Following the derivation in MAMW11, the time-scale for changes in angular momentum due to an enclosed distribution of stars with mass $m_\star$ acting as a coherent torque is

$$\tau_{\rm coh} = \frac{M_\bullet}{\sqrt{N(a)} m_\star} \Big(\frac{a^3 (1-e^2)}{G M_\bullet} \Big)^{1/2} . \tag{24}$$

The number of stars within a sphere delimited by the BHs semi-major axis, $N(a)$ is related to the density profile $\rho(r)$. For a general power law $\rho(r) \propto r^{-\gamma}$, the number of stars within a certain radius a becomes

$$N(r < a) = N_{<1} \tilde{a}^{3-\gamma} \,, \tag{25}$$

where $N_{<1}$ is the number of stars within a sphere of radius 1 mpc. The condition for the Schwarzschild barrier is that the relativistic precession time-scale, Eq. (7), becomes smaller than $\tau_{\rm coh}$, i.e.

$$a(1-e^2)^{1/2} = \frac{3G}{2\pi c^2} \frac{M_\bullet^2}{m_\star} \sqrt{N(r<a)} \,. \tag{26}$$

In our model with $\gamma = 2$ and $N_{<1} \approx 5$, we obtain the relation

$$N(r < a) \approx 5\, \tilde{a} \,, \tag{27}$$

and thus the barrier at

$$\tilde{a}_{\rm SB} \approx C_{\rm SB} (1-e^2)^{-1/3} \,, \tag{28}$$

where $C_{\rm SB} \approx 0.35$ in this particular order of magnitude comparison. This line is shown in blue in Fig. 2. The bottom-left side of it is the region where RR is inefficient. However, NR is still in play. The next delimiter is placed by the inspiral time-scale $\tau_{\rm GW}$. As soon as $\tau_{\rm GW} < \tau_{\rm NR}$, BHs decouple from the stellar background and inspiral gradually, driven by energy loss through gravitational radiation. The condition for this, using Eq. (10) and Eq. (2), yields

$$\begin{aligned} \tilde{a}_{\rm GW} \approx & 1.5 \times 10^{-2} \Big(\frac{M_\bullet}{10^6\, M_\odot} \Big) \Big(\frac{m_\star}{50\, M_\odot} \Big)^{-2/7} \\ & \times \Big(\frac{N_{<1}}{5} \Big)^{-2/7} (1-e^2)^{-5/7} \,. \end{aligned} \tag{29}$$

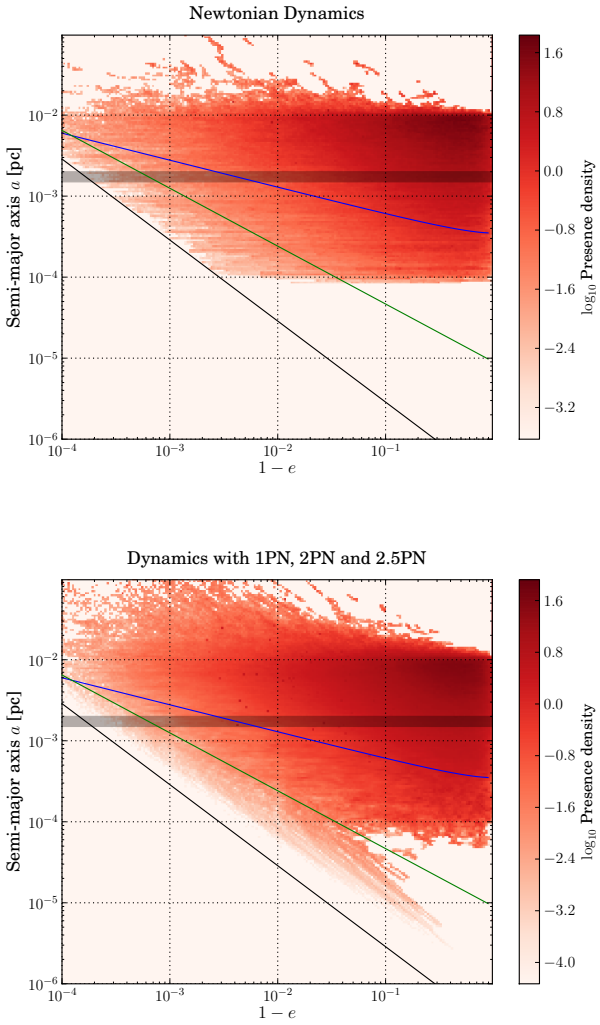

Figure 2. Integrated presence density for the Newtonian (set SI, top panel) and the relativistic case (set SIII, bottom panel). The shaded box marks the region of the slice analyzed in Fig. 3. The lines indicate the position of the Schwarzschild barrier with $C_{\rm SB} = 0.35$ (*blue*) and the limit for capture onto inspiral orbits for non-resonant relaxation (*green*).

This line for gravitational capture against non-resonant relaxation is shown in green in Fig. 2. The relativistic set (bottom panel) shows the characteristic inspiral lines, which cause the presence very close to the merger limit ($a < 6\,r_g$) to be depleted in comparison to the Newtonian case, where the particles are scattered into plunge orbits onto the MBH instead.

Fig. 3 shows the presence integrated over a small slice in semi-major axis (the shaded area in Fig. 2) for all the simulated sets. In this plot we show the location of the barrier at $C_{\rm SB} = 0.35$, shown as the blue region. Since we average over a certain part in the semi-major axis, the lines from Fig. 2 now appear as regions marking the lower and upper boundary at the limiting semi-major axis values.

The same decrease in presence density can be observed for the runs with no dissipative forces, set SIV and SV, which both show the same behavior towards high eccentricities. This confirms the validity of the PN approximation in this

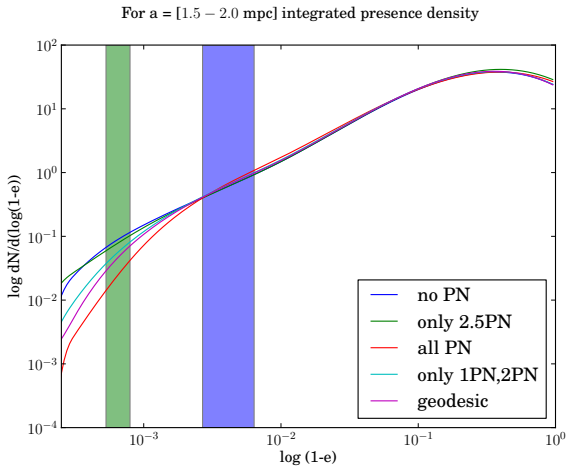

Figure 3. Integrated presence density for a semi-major axis slice $1.5\,\mathrm{mpc} < a < 2.0\,\mathrm{mpc}$. The shaded boxes represent the position of the Schwarzschild barrier with $C_{\rm SB} = 0.35$ (*blue*) and the threshold between the regime in which the evolution is dominated by dynamics and when the binary decays via gravitational loss (*green*)

.

Series	Plunge (yr^{-1})	Inspiral (yr^{-1})
SI: Newtonian	$(2.7 \pm 0.2) \times 10^{-5}$	–
SII: Only 2.5 PN	$(2.6 \pm 0.2) \times 10^{-5}$	$(4.3 \pm 0.6) \times 10^{-6}$
SIII: Full PN	$(8 \pm 1) \times 10^{-7}$	$(5 \pm 1) \times 10^{-7}$
SIV: 1PN, 2PN	$(1.5 \pm 0.1) \times 10^{-6}$	–
SV: Geodesics	$(1.4 \pm 0.1) \times 10^{-6}$	–

Table 1. Comparison of the different event rates for the different scenarios studied.

regime for our purposes. It also suggests that the system barely access the regime where the PN and geodesic dynamics differ, i.e. where the relativistic precession predicted by the geodesic equations of motion is significantly different from the 1PN and 2PN corrections.

The drop for set SIII as compared to IV and V is stronger, because of the presence of inspirals depleting the very high eccentricity region.

Set SI and SII also show consistent results. This was expected because the decoupling into inspiral orbits happens on length scales below the merger criterion for resonant relaxation, see Eq. (19).

We summarize the event rates for our idealized system in Table 1. Our rates are only meant to compare different sets of simulations and can only be read as absolute values for a real galactic nucleus.

5 DISCUSSION

Recently, Merritt et al. (2011) estimated with a few direct-summation $N-$body simulations expanded with a statistical Monte-Carlo study that the "traditional EMRI" event is

markedly decreased by the presence of a blockade in the rate at which orbital angular momenta change takes place. This so-called "Schwarzschild barrier" is a result of the impact of relativistic precession on to the stellar potential torques. Although the authors find that some particles can penetrate the barrier, EMRIs are significantly suppressed in this scenario.

In this study we investigated the effects of relativistic corrections on the event rates for EMRIs compared to Newtonian dynamics using a PN approach as presented in the original work of Kupi et al. (2006) but also and for the first time with the implementation of geodesic equations. For this purpose, we ran different sets of 500 simulations each, for combined durations of $\sim 100\,\mathrm{Myr}$ in order to obtain statistically solid results. We confirm the quenching of RR in the presence of Schwarzschild precession, i.e. the Schwarzschild barrier. Comparing full PN simulations (up to order 2.5) with the Newtonian ones, we find a ratio of the time-scales for the capture (combined plunge and inspiral) of

$$\tau_{\mathrm{GR}}/\tau_{\mathrm{Newtonian}} \approx 21 \pm 7 \tag{30}$$

and for the absolute value for our setup an EMRI event rate of $\lesssim 1\,\mathrm{Myr}^{-1}$. This value serves as an order of magnitude estimate for galactic centers similar to our idealized setup.

In order to investigate the validity of the barrier at high eccentricities and very small pericentres, we have implemented the geodesic equations of motion around the MBH as an alternative to the PN corrections. We find that the results we obtain from both methods are consistent although the relativistic precession they predict is significantly different near the last stable orbit. This suggests that the stellar dynamics of the systems we have studied does not access significantly the regime where the dynamics as described by the geodesic equations and the PN corrections is different. Therefore we deem it necessary to address the scenario to check whether these results are recovered when we increase the number of stars N. We hence plan on expanding the studied system for usage with $N-$body codes. This will allow us to investigate realistic galactic nuclei and thus make more precise statements about the absolute event rates to be expected.

We corroborate the existence of the "Schwarzschild barrier" and its impact on the rate at which orbital angular momenta change takes place *at these distances*. It is important to note that recently Amaro-Seoane et al. (2012d) proved that for Kerr MBHs, direct plunges are in reality high-eccentricity EMRIs, and that the rate in enhanced depending on the spin and inclination. Although our simulations probe only an idealized case in which we study a peculiar, though representative distribution, the consequences are clear: The event rate of EMRIs for a LISA-like mission such as eLISA (Amaro-Seoane et al. 2012a,b) will be dominated by high-eccentric EMRIs, which are not "direct plunges" if the central MBH is spinning. On the other hand EMRIs produced in the region in which it was believed that resonant relaxation could represent a significant enhancement in the rates, will suffer a drastic cut in the rates and, hence, they will be only a negligible contribution.

ACKNOWLEDGMENTS

This work has been supported by the Transregio 7 "Gravitational Wave Astronomy" financed by the Deutsche Forschungsgemeinschaft DFG (German Research Foundation). The simulations were run on the ATLAS cluster of the Albert-Einstein-Institute Hannover. CFS acknowledges support from the Ramón y Cajal Programme of the Spanish Ministry of Education and Science, contract 2009-SGR-935 of AGAUR, and contracts FIS2008-06078-C03-03, AYA-2010-15709, and FIS2011-30145-C03-03 of MICCIN. We acknowledge the computational resources provided by the BSC-CNS (contracts AECT-2012-1-0008 and AECT-2012-2-0014) and CESGA (contracts CESGA-ICTS-221 and ICTS-CESGA-234).

APPENDIX A: GEODESIC EQUATIONS FOR A PARTICLE ORBITING A BLACK HOLE

In this appendix we write down the geodesic equations of motion in a form that is suitable to be included in a N-body code that uses a Newtonian-type formulation of the equations of motion. In order to compare results with the cases where PN corrections are used we write the geodesic equations using harmonic coordinates for Schwarzschild, which are compatible with the harmonic gauge condition of PN theory.

Since our particles represent stellar objects we need to consider the geodesics for massive particles (i.e. timelike geodesics). Given our system of spacetime coordinates $\{x^\mu\} = \{t, x^i\}$ $(\mu, \nu, \cdots = 0-3;\ i, j, \ldots = 1-3)$, a geodesic will be given by $\{x^\mu(\tau)\}$, where τ denotes the particle's proper time. The components of the velocity vector are defined as

$$u^\mu = \frac{dx^\mu(\tau)}{d\tau}\,. \tag{A1}$$

This four-velocity vector satisfies:

$$g_{\mu\nu}u^\mu u^\nu = -c^2\,, \tag{A2}$$

where $g_{\mu\nu}$ is the Schwarzschild metric in our coordinate system and c denotes the speed of light. Since we are interested in geodesics, the velocity vector must satisfy the following equation of motion (Misner et al. 1973).

$$u^\nu \nabla_\nu u^\mu = 0\,, \tag{A3}$$

where ∇_μ denotes the canonical covariant derivative associated with the spacetime metric $g_{\mu\nu}$. Expanding this equation we have

$$\frac{du^\rho}{d\tau} + \Gamma^\rho_{\mu\nu}u^\mu u^\nu = 0\,, \tag{A4}$$

being $\Gamma^\rho_{\mu\nu}$ the Christoffel symbols associated with the spacetime metric $g_{\mu\nu}$. They are given in terms of the metric by:

$$\Gamma^\mu_{\alpha\beta} = \frac{1}{2}g^{\mu\nu}\left(\frac{\partial g_{\alpha\nu}}{\partial x^\beta} + \frac{\partial g_{\beta\nu}}{\partial x^\alpha} - \frac{\partial g_{\alpha\beta}}{\partial x^\rho}\right)\,. \tag{A5}$$

Using the splitting of time and space we can write the velocity vector as follows:

$$\vec{\boldsymbol{u}} = u^t\frac{\partial}{\partial t} + u^i\frac{\partial}{\partial x^i}\,, \tag{A6}$$

where $\{u^t, u^i\}$ are the velocity components in the $\{t, x^i\}$ coordinate system:

$$u^t = \frac{\partial t(\tau)}{\partial \tau}\,, \qquad u^i = \frac{\partial x^i(\tau)}{\partial \tau}\,. \tag{A7}$$

Therefore, on the trajectory of the particle we can write

$$u^i = \frac{dx^i(t)}{dt}\frac{\partial t}{\partial \tau} = v^i u^t \equiv \Gamma v^i\,, \tag{A8}$$

where v^i are the spatial components of the velocity

$$v^i = \frac{dx^i(t)}{dt}\,, \tag{A9}$$

and Γ is the general relativistic version of the special relativistic gamma factor, which is given in terms of the components of the spatial velocity and the metric tensor as:

$$\Gamma^2 = -\frac{c^2}{g_{tt} + 2g_{ti}v^i + g_{ij}v^i v^j}\,. \tag{A10}$$

which, in the weak-field limit ($g_{tt} \approx -c^2\,, g_{ti} \approx 0\,, g_{ij} \approx \delta_{ij}$), has the usual expression:

$$\Gamma^2 \approx \frac{1}{1-\frac{v^2}{c^2}}\,, \qquad (v^2 \equiv \delta_{ij}v^i v^j)\,. \tag{A11}$$

At this point, we can now adopt a Newtonian point of view by looking at the geodesic equations for the six quantities: $\{x^i(t), v^i(t)\}$, that is, for the spatial coordinates and spatial velocity components. They can be written as:

$$\frac{dx^i}{dt} = v^i\,, \tag{A12}$$

$$\frac{dv^i}{dt} = f^i_g\,, \tag{A13}$$

where the *forces*, f^i_g, are actually forces per unit mass, i.e. accelerations, since they should not depend on the mass of the body (according to the equivalence principle). Moreover, these specific forces depend on the spacetime metric (and its first derivatives) and on v^i. They can be written as

$$\begin{aligned} f^i_g =& v^i\,\Gamma^t_{tt} - \Gamma^i_{tt} + 2\left(v^i\,\Gamma^t_{tj} - \Gamma^i_{tj}\right)v^j \\ &+ \left(v^i\,\Gamma^t_{jk} - \Gamma^i_{jk}\right)v^j v^k\,. \end{aligned} \tag{A14}$$

Given initial conditions $\{x^i_o, v^i_o\}$ equations (A12,A13) have a unique solution $\{x^i(t), v^i(t)\}$. Note that the c^2 factor dividing the forces, when going to the right-hand side of the equation (multiplying the Christoffel symbols) will cancel the c^2 factor in the denominator of r_g [see expressions in Eqs. (A22)-(A27)].

Since up to now the development has been quite general, let us now consider the case of a non-spinning (Schwarzschild) MBH black hole of mass $M_\bullet$. The metric components, in harmonic coordinates, can be written in the following form:

$$g_{tt} = -\frac{1-\frac{r_g}{r}}{1+\frac{r_g}{r}}\,c^2\,, \tag{A15}$$

$$g_{ti} = 0\,, \tag{A16}$$

$$g_{ij} = \frac{1+\frac{r_g}{r}}{1-\frac{r_g}{r}}\,n_i n_j + \left(1+\frac{r_g}{r}\right)^2\left(\delta_{ij} - n_i n_j\right)\,, \tag{A17}$$

where

$$r = \sqrt{\delta_{ij}\,x^i x^j}\,, \qquad n^i = \frac{x^i}{r}\,, \qquad r_g = \frac{GM_\bullet}{c^2}\,. \tag{A18}$$

¿From here, the components of the inverse metric are:

$$g^{tt} = -\frac{1+\frac{r_g}{r}}{1-\frac{r_g}{r}}\,\frac{1}{c^2}\,, \tag{A19}$$

$$g^{ti} = 0\,, \tag{A20}$$

$$g^{ij} = \frac{1-\frac{r_g}{r}}{1+\frac{r_g}{r}}\,n^i n^j + \frac{1}{\left(1+\frac{r_g}{r}\right)^2}\left(\delta^{ij} - n^i n^j\right)\,, \tag{A21}$$

where $x_i = \delta_{ij}\,x^j$ and $n_i = \delta_{ij}\,n^j$.

The important thing to determine the forces is the computation of the Christoffel symbols. ¿From their definition (A5) we find the following result

$$\Gamma^t_{tt} = 0\,, \tag{A22}$$

$$\Gamma^t_{ti} = \frac{r_g}{r^2}\frac{n_i}{1-\left(\frac{r_g}{r}\right)^2}\,, \tag{A23}$$

$$\Gamma^t_{ij} = 0\,, \tag{A24}$$

$$\Gamma^i_{tt} = \frac{r_g}{r^2}\frac{1-\frac{r_g}{r}}{\left(1+\frac{r_g}{r}\right)^3}\,n^i\,c^2\,, \tag{A25}$$

$$\Gamma^i_{tj} = 0\,, \tag{A26}$$

$$\begin{aligned} \Gamma^i_{jk} =& \frac{r_g}{r^2}\frac{1}{1+\frac{r_g}{r}}\Big[\left(1+\frac{r_g}{r}\right)\,n^i\left(\delta_{jk} - n_j n_k\right) \\ &- \frac{n^i n_j n_k}{1-\frac{r_g}{r}} - 2n_{(j}\left(\delta^i_{k)} - n^i n_{k)}\right)\Big]\,. \end{aligned} \tag{A27}$$

And this determines completely the geodesic equations of motion in Eqs. (A12) and (A13).

Finally, we can make a post-Newtonian expansion of the equations of motion. That is, an expansion for $r_g/r \ll 1$, and $v/c \ll 1$. In our case, the expression for the *force* simplifies to [see Eq. (A14) and Eqs. (A22)-(A27)]:

$$f^i_g = -\Gamma^i_{tt} + 2\,v^i\,\Gamma^t_{tj}v^j - \Gamma^i_{jk}v^j v^k\,. \tag{A28}$$

Expanding this we get:

$$\begin{aligned} f^i_g =& -\frac{r_g c^2}{r^2}\left[1 - 4\frac{r_g}{r} + 9\left(\frac{r_g}{r}\right)^2 - 16\left(\frac{r_g}{r}\right)^3\right]\,n^i \\ &+ 2\,\frac{r_g c^2}{r^2}\left[1+\left(\frac{r_g}{r}\right)^2\right]\left(\frac{n_j v^j}{c}\right)\frac{v^i}{c} \\ &- \frac{r_g c^2}{r^2}\Big\{\,n^i\left(\delta_{jk} - n_j n_k\right) - \left[1+\left(\frac{r_g}{r}\right)^2\right]n^i n_j n_k \\ &- 2\left[1 - \frac{r_g}{r} + \left(\frac{r_g}{r}\right)^2 - \left(\frac{r_g}{r}\right)^3\right]n_{(j}\left(\delta^i_{k)} - n^i n_{k)}\right)\Big\} \\ &\times \frac{v^j}{c}\frac{v^k}{c}\,, \end{aligned} \tag{A29}$$

where the first two rows correspond to the first two terms in Eq. (A28). We have expanded in Taylor series the functions of r_g/r up to order $(r_g/r)^4$. We can now collect the terms

and we find the following expression, which is valid to order 2PN [see Eq. (B1) below]:

$$f_g^i = -\frac{GM_\bullet}{r^2}n^i + \frac{GM_\bullet}{r^2}\Big\{\left(\mathcal{A}_{1\rm PN}+\mathcal{A}_{2\rm PN}\right)n^i + \frac{\boldsymbol{n}\cdot\boldsymbol{v}}{c}\left(\mathcal{B}_{1\rm PN}+\mathcal{B}_{2\rm PN}\right)\frac{v^i}{c}\Big\}, \tag{A30}$$

where

$$\frac{\boldsymbol{n}\cdot\boldsymbol{v}}{c} = \frac{\boldsymbol{x}}{cr}\frac{d\boldsymbol{x}}{dt} = \frac{1}{2cr}\frac{d\boldsymbol{x}^2}{dt} = \frac{1}{2cr}\frac{dr}{dt} = \frac{\dot r}{c}, \qquad v^2 = \boldsymbol{v}\cdot\boldsymbol{v} = \delta_{ij}v^iv^j, \tag{A31}$$

and

$$\mathcal{A}_{1\rm PN} = 4\frac{r_g}{r} - \frac{v^2}{c^2}, \tag{A32}$$

$$\mathcal{A}_{2\rm PN} = -9\left(\frac{r_g}{r}\right)^2 + 2\left(\frac{\boldsymbol{n}\cdot\boldsymbol{v}}{c}\right)^2\frac{r_g}{r}, \tag{A33}$$

$$\mathcal{B}_{1\rm PN} = 4, \tag{A34}$$

$$\mathcal{B}_{2\rm PN} = -2\frac{r_g}{r}. \tag{A35}$$

APPENDIX B: PN CORRECTIONS

The PN equations of motion used in our simulations can be written in the form given in Eq. (11). We can organize the different terms in the following form (which is similar to the one used above in Eq. (A30) for geodesic equations):

$$f_g^i = -\frac{GM}{r^2}n^i + \frac{GM}{r^2}\Big\{\left(\mathcal{A}'_{1\rm PN}+\mathcal{A}'_{2\rm PN}\right)n^i + \frac{\boldsymbol{n}\cdot\boldsymbol{v}}{c}\left(\mathcal{B}'_{1\rm PN}+\mathcal{B}'_{2\rm PN}\right)\frac{v^i}{c} + \frac{\boldsymbol{n}\cdot\boldsymbol{v}}{c}\mathcal{A}'_{2.5\rm PN}\,n^i + \mathcal{B}'_{2.5\rm PN}\frac{v^i}{c}\Big\}, \tag{B1}$$

where here $M = m_\star + M_\bullet$ is the two-body (MBH+star) total mass. We list here the PN coefficients [see, e.g. (Blanchet 2006), Eq. (131)] for $m_\star \neq 0$:

$$\mathcal{A}'_{1\rm PN} = \frac{3}{2}\nu\left(\frac{\boldsymbol{n}\cdot\boldsymbol{v}}{c}\right)^2 - (1+3\nu)\frac{v^2}{c^2} + (4+2\nu)\frac{R_g}{r}, \tag{B2}$$

$$\mathcal{A}'_{2\rm PN} = -\frac{15}{8}\nu(1+3\nu)\left(\frac{\boldsymbol{n}\cdot\boldsymbol{v}}{c}\right)^4 + \nu(3-4\nu)\left[\frac{3}{2}\left(\frac{\boldsymbol{n}\cdot\boldsymbol{v}}{c}\right)^2 - \frac{v^2}{c^2}\right]\frac{v^2}{c^2} + \frac{R_g}{r}\Big\{2\left(1+\frac{25}{2}\nu+\nu^2\right)\left(\frac{\boldsymbol{n}\cdot\boldsymbol{v}}{c}\right)^2 + \nu\left(\frac{13}{2}-2\nu\right)\frac{v^2}{c^2}\Big\} - \left(9+\frac{87}{4}\nu\right)\frac{R_g^2}{r^2}, \tag{B3}$$

$$\mathcal{A}'_{2.5\rm PN} = \frac{24}{5}\frac{R_g}{r}\frac{v^2}{c^2} + \frac{136}{15}\nu\left(\frac{R_g}{r}\right)^2, \tag{B4}$$

$$\mathcal{B}'_{1\rm PN} = 4-2\nu, \tag{B5}$$

$$\mathcal{B}'_{2\rm PN} = -\frac{3}{2}\nu(3+2\nu)\left(\frac{\boldsymbol{n}\cdot\boldsymbol{v}}{c}\right)^2 + \nu\left(\frac{15}{2}+2\nu\right)\frac{v^2}{c^2} - \left(2+\frac{41\nu}{2}+4\nu^2\right)\frac{R_g}{r}, \tag{B6}$$

$$\mathcal{B}'_{2.5\rm PN} = -\frac{24}{5}\nu\left(\frac{R_g}{r}\right)^2 - \frac{8}{5}\nu\frac{R_g}{r}\frac{v^2}{c^2}. \tag{B7}$$

where ν is the symmetric mass ratio, $\nu = m_\star M_\bullet/M^2$, and $R_g = GM/c^2$. One can verify that the coefficients in Eq. (A32) to Eq. (A35) agree with Eq. (B2) to (B7) for $\nu = 0$.

REFERENCES

Aarseth S. J., 1999, The Publications of the Astronomical Society of the Pacific, 111, 1333

—, 2003, Gravitational N-Body Simulations. ISBN 0521432723. Cambridge, UK: Cambridge University Press, November 2003.

Amaro-Seoane P., 2012, ArXiv e-prints

Amaro-Seoane P., Aoudia S., Babak S., Binétruy P., Berti E., Bohé A., Caprini C., Colpi M., Cornish N. J., Danzmann K., Dufaux J.-F., Gair J., Jennrich O., Jetzer P., Klein A., Lang R. N., Lobo A., Littenberg T., McWilliams S. T., Nelemans G., Petiteau A., Porter E. K., Schutz B. F., Sesana A., Stebbins R., Sumner T., Vallisneri M., Vitale S., Volonteri M., Ward H., 2012a, Accepted for publication at GW Notes

—, 2012b, Classical and Quantum Gravity, 29, 124016

Amaro-Seoane P., Brem P., Cuadra J., Armitage P. J., 2012c, ApJ Lett., 744, L20

Amaro-Seoane P., Gair J. R., Freitag M., Miller M. C., Mandel I., Cutler C. J., Babak S., 2007, Classical and Quantum Gravity, 24, 113

Amaro-Seoane P., Sopuerta C. F., Dewi Freitag M., 2012d, ArXiv e-prints

Amaro-Seoane P., Spurzem R., 2001, MNRAS, 327, 995

Barth A. J., 2004, in Coevolution of Black Holes and Galaxies, from the Carnegie Observatories Centennial Symposia., Ho L., ed., Cambridge University Press, p. 21

Berry C. P. L., Gair J. R., 2012, ArXiv e-prints

Binney J., Tremaine S., 2008, Galactic Dynamics: Second Edition, Binney J., Tremaine S., eds. Princeton University Press
Blanchet L., 2006, Living Reviews in Relativity, 9, 4
de Zeeuw T., 2001, in Black Holes in Binaries and Galactic Nuclei, Proceedings of the ESO Workshop held at Garching, Germany, 6-8 September 1999., ESO Astrophysics Symposia, Springer, p. 78
Eisenhauer F., Genzel R., Alexander T., Abuter R., Paumard T., Ott T., Gilbert A., Gillessen S., Horrobin M., Trippe S., Bonnet H., Dumas C., Hubin N., Kaufer A., Kissler-Patig M., Monnet G., Ströbele S., Szeifert T., Eckart A., Schödel R., Zucker S., 2005, ApJ, 628, 246
Frank J., Rees M. J., 1976, MNRAS, 176, 633
Freitag M., Amaro-Seoane P., Kalogera V., 2006, ApJ, 649, 91
Genzel R., Eisenhauer F., Gillessen S., 2010, Reviews of Modern Physics, 82, 3121
Ghez A. M., Salim S., Hornstein S. D., Tanner A., Lu J. R., Morris M., Becklin E. E., Duchêne G., 2005, ApJ, 620, 744
Ghez A. M., Salim S., Weinberg N. N., Lu J. R., Do T., Dunn J. K., Matthews K., Morris M. R., Yelda S., Becklin E. E., Kremenek T., Milosavljevic M., Naiman J., 2008, ApJ, 689, 1044
Gillessen S., Eisenhauer F., Trippe S., Alexander T., Genzel R., Martins F., Ott T., 2009, ApJ, 692, 1075
Hopman C., Alexander T., 2005, ApJ, 629, 362
—, 2006, ApJ, 645, 1152
Kormendy J., 2004, in Coevolution of Black Holes and Galaxies, from the Carnegie Observatories Centennial Symposia., Ho L., ed., Cambridge University Press, p. 1
Kupi G., Amaro-Seoane P., Spurzem R., 2006, MNRAS, L77+
Lightman A. P., Shapiro S. L., 1977, ApJ, 211, 244
Magorrian J., Tremaine S., 1999, MNRAS, 309, 447
Merritt D., Alexander T., Mikkola S., Will C. M., 2011, Phys. Rev. D, 84, 044024
Misner C. W., Thorne K. S., Wheeler J. A., 1973, Gravitation
Peters P. C., 1964, Physical Review, 136, 1224
Rees M. J., 1988, Nat, 333, 523
Richstone D., 2004, in Coevolution of Black Holes and Galaxies, from the Carnegie Observatories Centennial Symposia., Ho L., ed., Cambridge University Press, p. 280
Sopuerta C. F., 2010, GW Notes, Vol. 4, p. 3-47, 4, 3
Spitzer L., 1987, Dynamical evolution of globular clusters. Princeton, NJ, Princeton University Press, 1987, 191 p.
Syer D., Ulmer A., 1999, MNRAS, 306, 35
Wang J., Merritt D., 2004, ApJ, 600, 149
Yunes N., Berti E., 2008, Ph. Rv. D, 77, 124006